

# Active Transonic Shock Control

Abraham. N. Gissen<sup>\*</sup>, Bojan Vukasinovic<sup>\*</sup>, Ari Glezer<sup>\*</sup>, Sivaram P. Gogineni<sup>†</sup>,  
Michael C. Paul<sup>‡</sup>, and Donald J. Wittich<sup>‡</sup>

<sup>\*</sup>Woodruff School of Mechanical Engineering, Georgia Institute of Technology, Atlanta, GA 30332-0405.

<sup>†</sup>Spectral Energies, 5100 Springfield Street, Suite 301, Dayton, OH 45431.

<sup>‡</sup>Air Force Research Laboratory, Directed Energy Directorate, Kirtland AFB, NM 87117.

**A transonic shock over a two-dimensional convex surface is indirectly manipulated in wind tunnel experiments by fluidic control of the shock-induced separated shear layer. Fluidic actuation is effected by a spanwise array of individually-controlled pulsed jets with a 1 ms scale. The flow upstream and downstream of the shock is characterized in detail using planar PIV and schlieren visualization that are accompanied by simultaneous surface pressure measurements, all of which are acquired phase-locked to the actuation waveform. Pulsed actuation leads to a momentary attachment of the separated shear layer which, in turn, effects a significant synchronized streamwise translation of the shock followed by a longer relaxation as the surface vorticity layer re-separates. Following the rapid displacement and distortion during the transitory onset of the actuation, the normal shock intensifies and transitions to a lambda shock when the actuation jets approach their full momentum. The present data show a strong correlation between the surface dynamic pressure and the shock position that is extracted from the PIV measurements. Furthermore, when the actuation is applied with a given jet velocity offset, the shock's nominal position is offset relative to the baseline flow (i.e., in the absence of actuation), and it continues to respond to time-dependent actuation relative to that offset position. These findings indicate that indirect control of shock induced separation can be exploited for shock stabilization and time-dependent positioning.**

## Nomenclature

$C_p$	=	Pressure coefficient
$C_q$	=	Control mass flow rate coefficient
$f$	=	Flow control frequency
$H$	=	Ramp height
$M$	=	Mach number
$p_{d_i} \ i=1-3$	=	Time-resolved pressure
$p_e$	=	Static pressure at the test section end
$p_i$	=	Static pressure upstream from the test section
$p_k \ k=1-15$	=	Static centerline pressures
$p_{ref}$	=	Static reference pressure
$T$	=	Flow control actuation period
$t$	=	Time
$U$	=	Mean streamwise velocity component

## I. Background

Compressibility effects, and, in particular, the appearance of shock waves in transonic and supersonic flows can lead to significant penalties in the performance of external (airframes) and internal (propulsion) aerodynamic systems. Shock wave boundary layer interactions (SWBLIs) have been associated with local, and sometimes global flow separation, and pronounced unsteadiness with significant energy and performance losses (e.g., increase in drag) and undesirable aeroelastic effects.<sup>1-4</sup>

The flow physics of the interactions of shock waves with surface boundary layers has been the subject of extensive investigations since the 1940s. The early investigations<sup>5-8</sup> established details of the complex nature of these interactions with laminar and turbulent boundary layers at transonic speeds. The interaction of an incident oblique

or normal shock wave (which can be caused by an irregularity in wall shape, such as a corner or a step) results in concomitant alteration of both the velocity distribution within the boundary layer and in the wave pattern in the external flow and is typically accompanied by a local flow separation downstream of the shock (e.g., Adamson and Messiter<sup>9</sup>). In particular, the interactions of shock waves with turbulence can lead to substantial unsteadiness and deformation of the shock while the characteristic velocity, timescales and length scales of turbulence change considerably.<sup>10</sup>

The study of these transonic embedded shocks have been well studied with their fundamental characteristics the subject of numerous investigations such as Liu<sup>11</sup>, where holographic interferometry was used to visualize the shockwave and resulting separation. More detailed studies carried out to investigate the properties of the shock boundary layer interaction at transonic speeds were performed by Delery.<sup>12</sup> An updated and extended treatment of a similar phenomenon using modern techniques can be found in Sartor et al.<sup>13</sup> Investigation of the unsteadiness associated with more complex three dimensional flows have been experimentally investigated by a number of authors such as Beresh et al.<sup>14</sup> A recent comprehensive overview of shock wave unsteadiness has been collected by Poggie et al.<sup>15</sup>

The influence of shock waves on transonic flow over airfoils was of much interest due to unfavorable flight characteristics of traditional subsonic airfoils,<sup>16</sup> most notably efforts to better understand the ‘pitch-up phenomenon’, and gain a better understanding of shock induced drag. The adverse effects of shock boundary layer interactions have prompted much interest in their mitigation using flow control approaches (e.g., Dolling<sup>12</sup>) with varying degrees of effectiveness. Conventional flow control approaches applied to a variety of situations were reviewed in extensive detail by Pearcy<sup>1</sup>, including, relevant to the current study, a section which reviews boundary layer control applied to a half-airfoil or a ‘bump’. An overview of shock control strategies is provided by Delery<sup>2</sup>, including passive (use of vortex generators and local changes in surface contour) and active (suction and blowing or bleed at the surface, surface cooling) control. The author noted that some of these techniques can be used to either modify the boundary layer upstream of the shock to increase its “resistance” to separation, or can be applied underneath or immediately downstream of the shock. A comprehensive review of early work on the suction and blowing for controlling shock boundary layer interactions was later presented by Viswanath<sup>3</sup>. Several authors (e.g., Lin<sup>18</sup>) described suppression of shock boundary layer separation by the introduction of streamwise vorticity upstream of the shock using low-profile, sub-boundary layer (ramp and vane) configurations of vortex generators (VGs). Ashill et al.<sup>19</sup> reported simultaneous increase in lift and decrease in drag by placing the VGs upstream of a normal shock on an airfoil in transonic flow. Vortex generators placed upstream from a compression corner were successful in reducing fluctuations associated with shockwave unsteadiness.<sup>20</sup> A comprehensive review of oscillations over transonic airfoils and methods to mitigate their effect can be found in Lee,<sup>21</sup> and a review of recent experimental results focusing on complex interactions and their influence on shock wave behavior by Gaitonde.<sup>22</sup> Other passive methods applied to shock boundary layer interactions, shown to reduce drag, are porous surfaces and slots. These, along with a number of other flow control techniques designed to reduce wave drag, were explored in the EuroShock II project, the results of which were compiled and edited by Stanewsky et al.<sup>23</sup> Holden and Babinsky<sup>24</sup> showed that both ramp and vane VGs significantly suppressed separation induced by a normal shock within a test section duct at  $M = 1.5$ . However, the authors noted that the VGs which were placed directly underneath the shock also increased the wave drag. In a recent numerical study, Lee et al.<sup>25</sup> demonstrated suppression of separation induced by a terminating normal shock within a diffuser ( $M = 1.3$ ). Passive flow control, in the form of an upstream fence, was shown to have an effect on the aero-optical environment of shock induced separated flow.<sup>26</sup>

Active flow control approaches based on continuous suction and blowing have also been applied for mitigation of shock-induced separation by modification of the boundary layer upstream of the shock. Wallis and Stuart<sup>27</sup> demonstrated the use of vortex generating jets on an airfoil-shaped surface to reattach separated flow, where the streamwise vorticity generated is shown to have favorable effects both upstream and downstream of the transonic shock. It is notable that their efforts resulted in translation of the shock wave position over a range of pressure ratios. Englar<sup>28</sup> investigated several different blowing strategies applied to elliptic airfoils at transonic speeds showing, using lift and drag comparison, that tangential blowing over an elliptical surface provided the best performance. Krogmann et al.<sup>29</sup> demonstrated that high-aspect ratio suction upstream of a normal shock over an airfoil in transonic flow ( $M = 0.78$ ) at off-design conditions led to reduction in the boundary layer thickness and improved the overall aerodynamic performance by delaying the rapid growth of the separation bubble and stabilizing the shock. These authors noted that even the inactive suction slots (and underlying cavity) had significant beneficial effects in terms of reduction in separation and buffeting ostensibly due to coupled cavity feedback. Souverein and Debieve<sup>30</sup> used a spanwise array of sub-mm, continuous jets for generation of streamwise

vorticity for suppression of boundary layer separation induced by an oblique-shock on a test surface at  $M = 2.3$ , and noted that the reduction in the characteristic scale of the separation bubble was accompanied by an increase in the frequency of the energetic spectral components of the reflected shock.

More recently, the effectiveness of novel flow control technologies for mitigation of adverse shock boundary layer interactions has been investigated. Kalra et al.<sup>31,32</sup> conducted numerical and experimental studies of magneto-gasdynamics plasma actuators where directional (streamwise-oriented) plasma actuation is effected by a magnetic field. They reported reduction in the separated region with best results when the plasma actuator was positioned at the shock impingement zone. Another approach for controlling an oblique shock was presented by Narayanaswamy et al.,<sup>33</sup> who used a thermally driven synthetic jet (using electric discharge) to lock the shock-wave oscillations to the jet pulsating frequency (about 2 kHz) indicating potential for shock stabilization at higher actuation frequencies. For a comprehensive discussion of shock wave boundary layer interactions and their control see a review by Babinsky and Harvey.<sup>34</sup> Vukasinovic et al.<sup>35</sup> recently explored two active flow control approaches, namely ‘direct’ and ‘indirect’, for the transonic shock and its coupled flow separation control, with an emphasis on the large scale unsteadiness of the separated flow. This initial effort was followed by Gissen et al.<sup>36</sup> who established direct relationship between the streamwise displacement of the shock and the flow control coefficient for the indirect active flow control by a spanwise array of fluidic oscillating jets, operating over a broad range of Mach numbers.

The primary goal of the present investigation is to assess the effectiveness of indirect, active flow control of the static and dynamics characteristics of a transonic shock. The flow control approach focuses on the shock-induced flow separation (downstream of the shock), rather than on the shock itself. The global flow features in the absence and presence of actuation are characterized using a rounded ramp surface geometry, which induces a transonic shock and allows for shock motion in the absence of surface discontinuities.

## II. Experimental Setup and Diagnostics

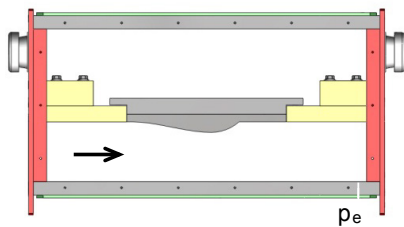


**Figure 1.** Schematics of the wind tunnel test section.

The present experiments were performed in a small, open-return pull-down high-speed subsonic wind tunnel driven by a 150 HP blower. The schematic of the test section is shown in Figure 1. The modular test section measures  $12.7 \times 12.7 \times 61$  cm, and the temperature of the return air is controlled using a chiller coupled with an ultra-low pressure drop heat exchanger. Two static pressure ports and a temperature probe are integrated into the tunnel wall for calibration and monitoring purposes. The first pressure port  $p_i$  and the temperature sensor are positioned immediately downstream from the tunnel inlet contraction, upstream from the test section. The second pressure port  $p_e$  is placed just upstream from the test section exit plane (Figure 1). The test section

having a nominal square cross section is calibrated using a Pitot probe at its center. The calibration is done relative to the pressure drop across the inlet contraction ( $\Delta p = p_{ig}$ ). The test section Mach number could be raised up to about  $M = 0.74$  in the absence of any test model.

A detailed layout of the 2-D test geometry, along with integrated diagnostic components, is shown in Figure 2a. The upper, nominally flat, wall of the test section is fitted with a gradual ramp that terminates as an aft surface of the radius  $4H$  ( $H = 20$  mm) that extends up to  $L = 2.6H$  past the apex. This aft geometry is selected as a generic convex surface that induces a localized shock formation in transonic flow conditions, and is adequate for studying the flow dynamics related to separated flows induced by the boundary layer separation in both adverse pressure gradient and

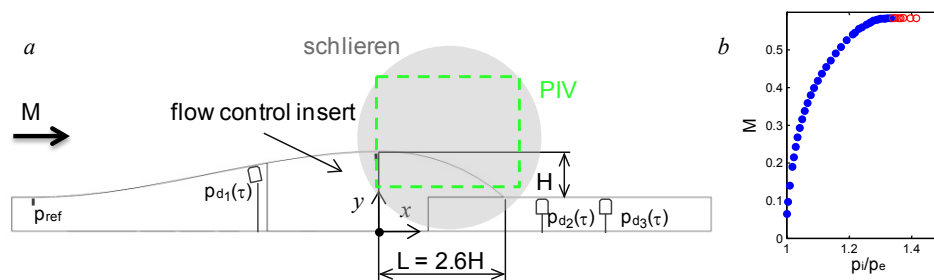


**Figure 2.** Schematics of the flow geometry and diagnostics (a), and the corresponding upstream Mach number with the pressure ratio  $p_i/p_e$  (b).

the shock-boundary layer interaction. Although assessing its full dependence is outside of the scope of the present study, it can be argued that the resulting shock dynamics would also be dependent on the actual surface curvature due to the altered pressure gradients.

The model geometry is composed of three sections, such that the first one consists of part of the ramp, the second is the main interchangeable section that can have the control devices built into it, and the third one represents the downstream wall. All of the model sections integrate into the upper wall of the tunnel test section. Only the nominal (without integrated flow control) central interchangeable section has fifteen static pressure ports distributed along the model centerline ( $p_1$ – $p_{15}$ ). Besides the static pressure measurements, three dynamic pressure sensors are flush-mounted along the centerline, one upstream  $p_{d1}$  and two downstream  $p_{d2}$  and  $p_{d3}$  from the model geometry at  $x/H = -2.95$ ,  $3.97$ , and  $4.96$ , respectively. The baseline and controlled flow fields are characterized by planar high-speed PIV measurements (field of view shown in Figure 2a), where each set of data is recorded at 2,800 fps. The mean flow fields and the statistics derived from the instantaneous velocity fields are based on ensembles of 2,700 image pairs, while the phase-averaged statistics is based on about 500 image pairs. For convenience, all PIV flow fields are shown in an inverted view. Lastly, the flow fields were characterized by schlieren visualization, where its field of view is centered about the aft section of the ramp, as schematically shown in Figure 2a. The single-pass schlieren setup incorporated a continuous light source passing through the 500  $\mu\text{m}$  pinhole. The schlieren images were captured by a digital camera at 15 fps and at an exposure time of 5  $\mu\text{s}$ .

The nominal flow over the test geometry was first characterized by the upstream ( $p_i$ ) and downstream ( $p_e$ ) pressure measurements over a full range of tunnel speeds, and its detailed characterization was previously shown by Gissen et al.<sup>36</sup>. As the tunnel chokes past the critical pressure ratio, it is proposed that the pressure ratio  $p_i/p_e$  is used to characterize the flow state throughout both flow regimes. Figure 2b depicts a relationship between the test section Mach number and the pressure ratio  $p_i/p_e$  for the present flow geometry. It is seen that, with an increase in pressure ratio, Mach number asymptotically approaches the choked condition, which is marked in red.

The planar high-speed PIV measurements are used to extract the instantaneous shock wave position, along with the full flow field assessment. First, it should be noted that due to the high laser intensity necessary for the high-speed PIV, intense surface reflections masked the flow ‘strip’ immediately near the surface in spite of the surface anti-reflective treatments. Therefore, all the measured flow fields exclude the near-wall region, which is masked hereafter, as illustrated in Figure 3a. Also, the full PIV fields of view spread across the edge of the optical window which very edge is captured in the upper right corner of the (inverted) flow field, and that corner is also masked in the presented flow fields. To extract the shock positions, horizontal component of velocity field is first plotted at each discretized elevation  $y/H$ , such as the one marked by the dashed line in Figure 3a. The corresponding instantaneous velocity traces are overlaid in Figure 3b in grey with the average velocity plotted in red for clarity. All velocity fields are shown relative to the reference velocity  $U_{\text{ref}}$  of the oncoming flow at the choking condition. When a shock wave is present in the flow field, the velocity ‘jump’ across the shock is quite distinguishable. The shock wave position for each particular elevation  $y/H$  is defined by finding the peak slope within the velocity ‘jump’ region. This process is repeated for all flow fields for all discretized  $y/H$  elevations and all of the shock positions are displayed on top of a time-averaged raster plot of the streamwise velocity in Figure 3a. These extracted shock detections illustrate a full domain of the baseline shock motion at the given pressure ration  $p_i/p_e = 1.34$  and also indicate an increase in shock deflections away from the wall. If all of the shock realizations are also spatially averaged, its mean position (shape) is obtained, which is shown in Figure 3c for this flow condition.

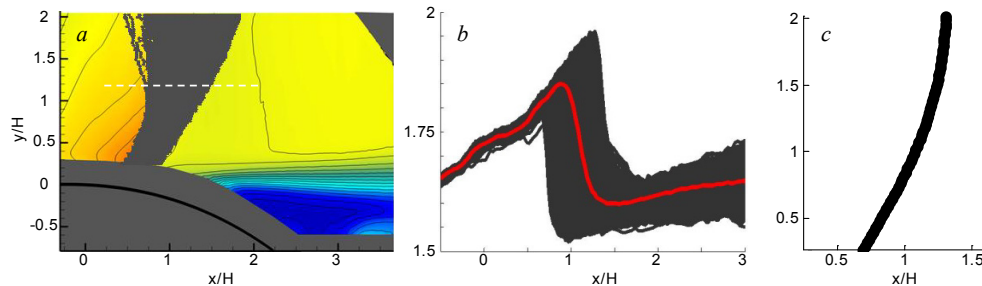


**Figure 3.** Overlapped discretized shock positions for the baseline flow at  $p_i/p_e = 1.34$  (a), the corresponding streamwise velocity profiles across the shock at the marked elevation (b), and extracted mean shock shape (c).

Instead of passive control devices typically used in the control of transonic shocks,<sup>34</sup> the present work utilizes active flow control elements, pulsed jets. The primary reason for incorporation of such jets is that they have a clear phase reference with respect to their cycle of operation, as opposed to the previously tested fluidic oscillating jets<sup>36</sup> that rely on natural, self-excited oscillations. The control of the phase of any individual jet also opens a possibility for the jets asynchronous operation, operation out of phase, and any other referencing of the jet phase to external processes; such could be adaptive optics, for instance. The pulsed jets in the present work are integrated into the surface geometry in exactly the same manner as the fluidic oscillating jets,<sup>36</sup> and they utilize the same air supply. Seven pulsed-jet actuators are equidistantly distributed across the model span past the apex. Each jet orifice is  $1.5 \times 1.5$  mm and neighboring jets are spaced 7.5 mm apart. Besides the clear phase reference in operation of the pulsed jets, there is a fundamental difference in operation relative to the oscillating jets: while the fluidic oscillating jets convert continuous air supply into unsteady oscillating jet due to internal flow resonance, the pulsed jets are set to operate at a half-duty of the actuation cycle, as the air is expelled through the orifice only during one half of the actuation cycle. However, both of these control elements combine the benefits of unsteady flow control due to their oscillating/pulsed nature and a net added mass and momentum to the flow, which is also assisted by the Coanda effect over the curved surface.

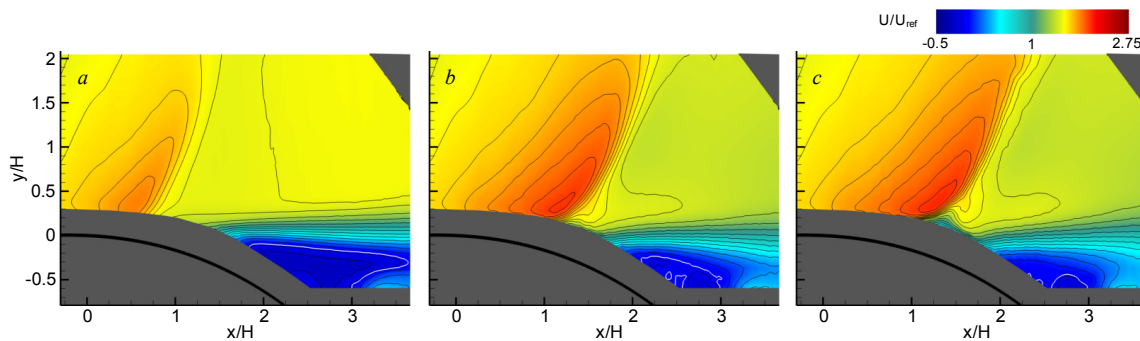


**Figure 4.** Raster plot of the mean streamwise velocity component for the baseline flow (a,  $p_i/p_e = 1.34$ ), and fully-open jet control at  $C_q \times 10^3 = 1.7$  (b), and 2.8 (c).

Prior to characterization of the pulsed jet effects, the installed array of jets is tested under the fully-open mode of operation, thus rendering the jets steady, without pulsing. This initial test is used for assessment of an ‘asymptotic’ effect of the control jet array. As an illustration of such an effect, three steady-state control effects are shown in Figure 4, along with the baseline flow field at  $p_i/p_e = 1.34$  shown in Figure 4a. In principle, a similar overall effect on the flow field is seen to the fluidic jet counterparts:<sup>36</sup> with an increase in the (equivalent) pulsed jets mass flow rate coefficient  $C_q$ , defined as a ratio between the total mass flow rate through the control jets and the mass flow rate through the test section, as the flow control reattaches the separated flow, the altered pressure field feeds back to the shock, which adjust according to the modified pressure field and thereby becomes displaced downstream. Along with its displacement, the shock gains in strength and develops a localized zone near the surface where the flow slows down behind the shock, but then continues to accelerate as the flow remains attached (Figure 4c). These shock dynamics are further examined and discussed in the schlieren visualization below.

After the expected ‘asymptotic’ flow control effect is established, the pulsed jets are then characterized in terms of their velocity distribution over the actuation cycle, in the absence of the outer flow. This jet calibration is done in situ with the wind tunnel inactive, where a miniature hot-wire sensor is placed at the jet center. The jet’s velocity is sampled simultaneously with the jet trigger signal, for the phase-referencing. Figure 5 shows the phase-averaged jet velocities over the jet full period of operation for the jet operation frequencies  $f = 100 - 900$  Hz. There are several notable features of the jet operation at the tested frequencies. First, only the jet operation at the lowest frequency realizes both end states, where jet attains its peak operational velocity and fully terminates upon the termination of the half-active cycle. As the trigger is applied, there is a short delay of about  $t/T = 0.05$  before the jet begins to be issued through the orifice. Also, once being issued, the jet reaches its near-peak velocity, after a

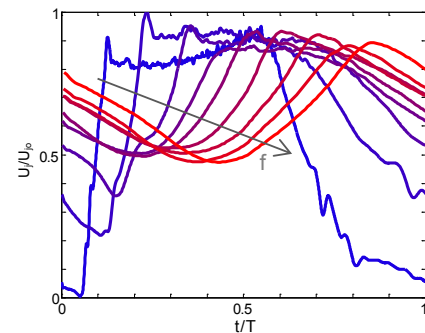


**Figure 5.** Pulsed jet velocity distributions during the operation cycle at  $f = 100 - 900$  Hz.

slight overshoot, at about  $t/T = 0.15$ . As the active part of the cycle continues to  $t/T = 0.5$ , the jet continues to build up and its termination slightly lags the control signal, as the jet velocity begins to decay at about  $t/T = 0.54$ . Although the most of the jet termination is completed by  $t/T = 0.8$ , its final leg lingers all the way to the end of the cycle. Given the described jet evolution under  $f = 100$  Hz, it is expected that the jet would not be fully terminated at higher frequencies. Thus, the next two operation frequencies show similar jet dynamics to  $f = 100$  Hz, but with an offset in the lowest velocity: as the jet from the previous operational cycle becomes suppressed, the next cycle commences and there is not sufficient time for its full termination. It is interesting, though, that all the remaining higher frequencies of operation show similar quasi-sinusoidal jet cycle, which essentially represents an quasi-sinusoidal ‘AC’ jet operation about a ‘DC’, steady jet effect. In other words, the higher frequency jet operation can be seen as superposition of steady and unsteady jets. The jet operating frequency  $f = 280$  Hz is selected as a nominal frequency at which the flow control effects are assessed in the present work. The jets’ time-resolved velocity is related to an ‘equivalent’ mass flow rate through the jets, and the flow control parameter is thereby expressed in terms of the mass flow rate coefficient  $C_q$ .

It is seen in Figure 5 that the jet onset somewhat lags the commanded signal, just as the jet decay trails the control signal termination. In order to establish proper phase references during the active flow control application, it is necessary to track a relevant parameter of the jet operation, besides the square control signal. As tracking the actual jet velocity not only impractical but would also require the hot wire holder presence in the channel flow and its probe aligned with the jet orifice, it is decided that the current associated with the jet cycle operation is monitored and recorded during the flow control investigations. Relationship between the “jet” current and jet velocity is illustrated in Figure 6, along with the sampled dynamic pressure signals at  $p_i/p_e = 1.34$ , during a single actuation cycle. The two traces clearly indicate that the jet begins to increase in velocity at the peak of the current signal (marked as *A*), while the onset of the jet velocity decay coincides with the current full termination (marked as *B*). In addition to this assessment, the sampled pressure data indicate that the shear layer / flow separation changes in response to the jet actuation are sufficient to be captured by the two downstream pressure sensors,  $p_{d2}$  and  $p_{d3}$ . Furthermore, it is also interesting to note that any downstream change in pressure does not propagate upstream far enough to be captured by the upstream sensor  $p_{d1}$ . In addition, there is no significant upstream disturbance to the oncoming boundary layer and the recorded pressure by  $p_{d1}$  is steady at all times, for a given flow condition.

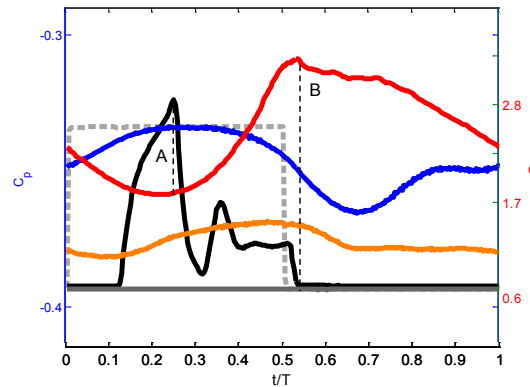


**Figure 6.** Dynamic response of the jet velocity (—) and pressure transducers  $p_{d1}$  (—),  $p_{d2}$  (—), and  $p_{d3}$  (—) during a single pulsed-jet actuation cycle (\*\*\*,  $f = 500$  Hz) at  $p_i/p_e = 1.34$ .

### III. The Baseline Flow

As the pressure ratio across the test section is increased, the flow over the convex surface becomes dominated by shock wave induced separation, which is of primary interest for the current study. Before this transition, the flow over the ramp results in subsonic separation induced by the adverse pressure gradient. Prior to the shock formation, the flow accelerates up to the ramp apex and then decelerates up to the point that the growing boundary layer cannot withstand the adverse pressure gradient. Contrary to this scenario, when the critical Mach number is reached at the apex, the flow continues to accelerate and terminates in a shock, where the underlying shock-boundary layer interaction induces discontinuous boundary layer thickening which, combined with the adverse pressure gradient, induces its ‘premature’ separation off the surface. Besides the related increase in the separated flow domain downstream from the incipient separation under the transonic shock, an additional difference relative to the subsonic separation is that the shear layer growth is aggressive, thus opening the upper boundary of the separated region and thereby enlarging the separated flow domain more compared with the subsonic flow over the ramp.

Baseline flow characterization is first done by the static pressure measurements along the ramp centerline and schlieren visualization. A dedicated computer-controlled *Scanivalve* pressure scanner was used for the pressure measurements. The pressure ports’ coordinates are defined relative to the apex of the contraction ( $x/H = 0$ ), and hence the pressure ports’ negative coordinates indicate their upstream position relative to apex. All the static



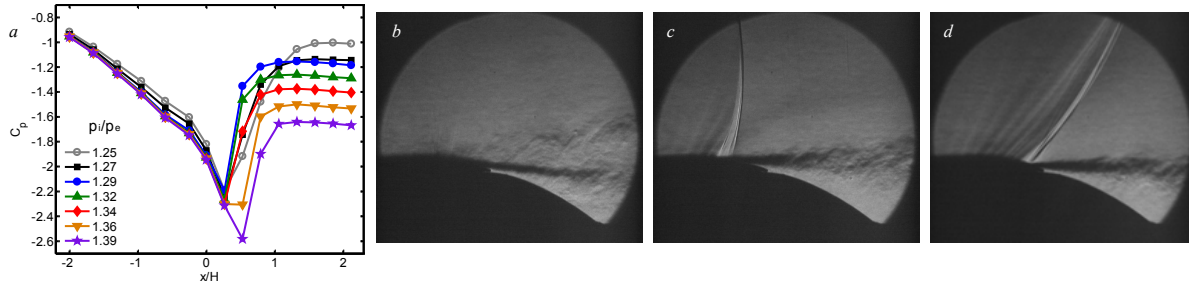


**Figure 7.** Baseline surface static pressure profiles with increasing  $p_i/p_e$  (a), and schlieren visualization of the flow at  $p_i/p_e = 1.25$  (b), 1.34 (c) and 1.45 (d).

pressures are shown in terms of the compressible pressure coefficient  $C_p$ , where the reference pressure  $p_{ref}$  (Figure 2) and the oncoming Mach number  $M$  are used as the reference parameters.

Figure 7a shows the measured surface pressure profiles for the varying tunnel speeds, where all but the lowest pressure ratio flow condition induce a transonic shock formation. The array of pressure profiles upstream from the apex indicate a typical evolution over a mildly converging surface, while downstream from the apex the flow becomes fully separated by about  $x/H = 1.5$ , for the subsonic separation at the lowest pressure ratio. The initial formation of the shock ( $p_i/p_e = 1.27$ ) seems to shift the flow separation upstream but not to lock it to the shock position, apparently as the boundary layer thickening due to the shock interaction is still not sufficient to induce momentary separation. Finally, at the pressure ratio  $p_i/p_e = 1.29$ , the flow separation moves further upstream locking to the shock position, clearly marking the shock-induced flow separation. It is interesting to note that the separation point moves downstream with a further increase in the pressure ratio. Therefore, the separation point moves upstream at the transition from subsonic to transonic flow regime, but then continuously shifts downstream with a further increase in the pressure ratio. Additional global characteristics of the baseline flow are illustrated in the corresponding schlieren images shown in Figure 7b–d. Figure 7b illustrates the flow condition at the lowest pressure ratio  $p_i/p_e = 1.25$ . The flow is clearly subsonic and the separated flow past the apex forms a shear layer, marked by the strong density gradients, which evolves downstream somewhat following the surface curvature at separation. Figure 7c shows a fully-formed normal shock past the critical point ( $p_i/p_e = 1.34$ ), and the clear coupling between the shock root and the shear layer origin points to the shock-induced separation that significantly opens up the near wake behind the ramp. As the upstream pressure ratio is increased, the shock gradually gains in strength, slants and extends further outward, towards the opposite wall. It is notable that the shock also begins to tilt slightly forward, which becomes increasingly prominent with further decrease of the back pressure. Eventually, the shock extends to the opposite test section wall, rendering the tunnel flow choked. As already stated, the flow mass rate does not change in the choked regime, and further increase in the pressure ratio only lowers the tunnel pressure downstream from the shock. The shock location also shifts somewhat downstream, as already seen in the separation point shift in Figure 7a. As a representative of the shock in the choked regime, Figure 7d shows the resulting flow condition at  $p_i/p_e = 1.45$ . The shock is fully tilted and displaced downstream compared to the state shown in Figure 7c.

Further illustration of the two transonic shock states is shown in Figures 8a and b, where a ‘waterfall’ representation of the horizontal velocity profiles is extracted from the PIV-measured flow fields for the

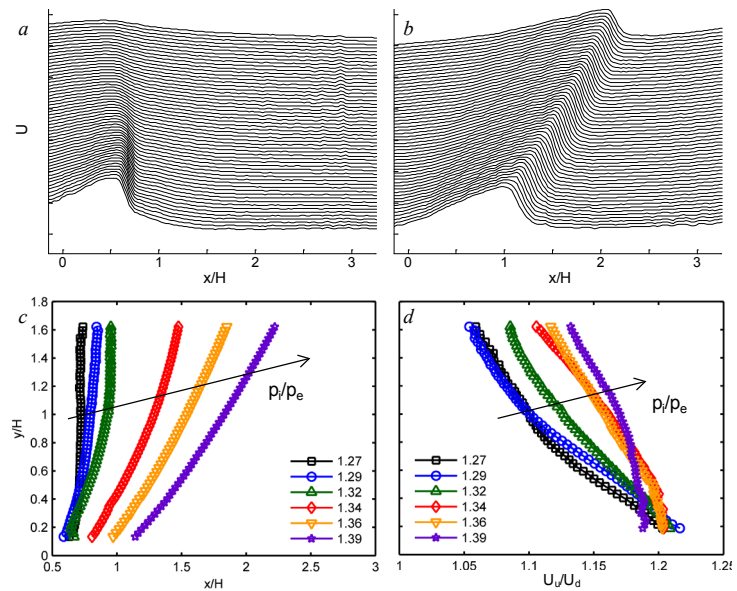


**Figure 8.** Streamwise ‘waterfall’ velocity profiles for the transonic shock at  $p_i/p_e = 1.27$  (a) and 1.39 (b), and the shock evolution in shape and position (c) and ‘strength’ (d) with  $p_i/p_e$ .

two flow states  $p_i/p_e = 1.27$  and  $1.39$ , representing the pre-choked and choked flow regimes, respectively. A strong velocity gradient is measured near the root of the normal shock in Figure 8a, which relaxes outward from the wall, as the shock is clearly localized near the surface. Contrary to this case, as the flow is choked, the velocity gradient across the shock appears more uniform, having a shallower gradient near the surface. Figure 8c shows the PIV-extracted shock profiles over a range of the pressure ratios  $p_i/p_e$ . It is interesting to note that the shock root displacement is minimal with an increase in  $p_i/p_e$ , as long as the flow is not choked. The only major effect on the shock is expressed in the shock slight increase in tilt with  $p_i/p_e$ . However, once the flow is choked, the shock displacement, with further increase in  $p_i/p_e$  becomes much more prominent, accompanied with progressive tilting. Another look at the effect on the transonic shock by the varying  $p_i/p_e$  is presented in Figure 8d. The ratio between the flow streamwise velocity upstream and downstream from the shock is chosen as a measure of the shock ‘strength’, and calculated at all measured elevations above the surface. Such profiles of the shock strength are shown in Figure 8d for the cases corresponding to those in Figure 8c. The pre-choked regime is characterized by the strong shock at its root, which rapidly diminishes away from the surface. As the  $p_i/p_e$  is increased within this regime, the shock strength proportionally increases for all observed elevations. Once the flow is choked, there are two notable alterations in the shock strength: its strength near the root begins to decrease, while it significantly increases away from the surface, rendering the shock strength more uniform in the outward direction.

Figure 9 summarizes both the shock shape/position and strength, as the pressure ratio across the test section is increased. A full range of the registered shock motion is marked by its upstream and downstream bounds, and this domain is colored by the corresponding contour plots of the local shock strength, i.e., the streamwise velocity ratio upstream and downstream from the shock. At the lowest pressure ratio (Figure 9a), the shock gains strength as it becomes displaced in the downstream direction, and a sharp gradient away from the wall is measured within the shock displacement bounds. As the pressure ratio is increased (Figure 9b), the shock tilt in the downstream direction becomes more pronounced, which is accompanied by a slight weakening near the root. A peak in the shock strength is measured approximately along the central shock position within the band. Further increase in the pressure ratio (Figure 9c) shows clear weakening of the shock in the downstream direction, while its gradient away from the surface becomes less pronounced, i.e., relaxed. Finally, for the highest pressure ratio in the choked regime, the shock exhibits a clear weakening as it moves in the downstream direction, with further increase in tilt and diffusion of the sharp gradients of velocity ratios across the shock.

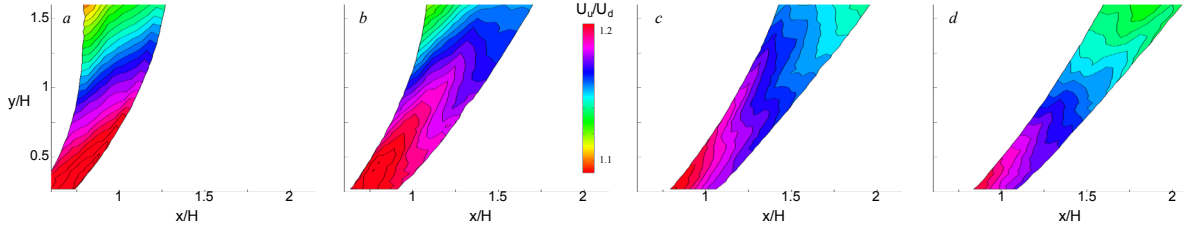


**Figure 9.** Contour plots of the shock ‘strength’  $U_u/U_d$  for  $p_i/p_e = 1.32$  (a),  $1.34$  (b),  $1.36$  (c), and  $1.39$  (d).

#### IV. The Controlled Flow

The present active control approach builds on the previous work by Gissen et al.<sup>36</sup>, where the transonic shock was manipulated by control of the separated flow resulting from the shock wave and boundary layer interaction by an active flow control approach utilizing fluidic oscillating jets. Such a control approach relies on the coupling between the shock, incipient boundary layer separation and the large-scale unsteadiness of the separated flow. When the flow control is capable of affecting the flow separation by altering its dynamic and static (mean) properties, the corresponding altered pressure field couples to the shock and also affects its static and dynamic characteristics. The present investigation utilizes such an active flow control approach by implementation of the pulsed jets, characterized in Section II, as active flow control components.

First, the overall, global effect of this active flow control is assessed by analysis of the mean flow field alteration. The mean flow fields for  $p_i/p_e = 1.34$  are shown in Figure 10 as contour plots of the mean streamwise velocity for the baseline, and the flow controlled by  $C_q = 2.8 \times 10^{-3}$  pulsed jets. Although the ensemble-averaged flow fields inevitably diffuse and relax the measured shock wave due to its unsteady nature, it is still informative to assess the averaged shock and separation location in each of the cases, as well as their impact on the shear layer. As it was already visualized in Figure 7c, the baseline flow shock-induced separation (Figure 10a) results in a nearly-horizontal shear layer that opens up into a significant domain of separated flow downstream from the ramp. The



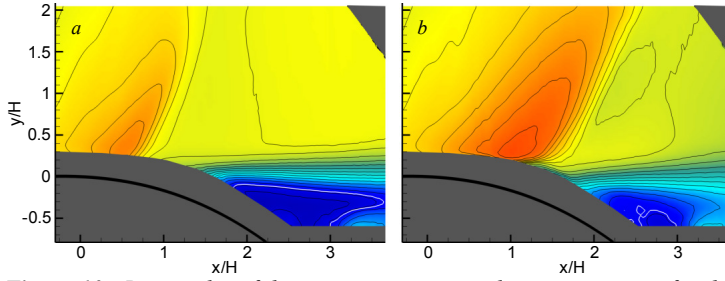


**Figure 10.** Raster plot of the mean streamwise velocity component for the baseline flow (a,  $p_i/p_e = 1.34$ ), and the flow controlled by the pulsed jets at  $f = 280$  Hz and  $C_q = 0.0028$  (b).

To further quantify the shock static and dynamic alteration under the flow control, the mean shock shape and its RMS oscillations about the mean position are plotted in Figure 11 for the two baseline and controlled flow shown in Figure 10. In addition, the two resulting shock alterations under the steady jets operated at  $C_q \times 10^3 = 1.7$  and 2.8 (Figure 4b and c, respectively) are also shown for reference. These steady-jet cases are selected as they introduce about the same shock displacement, on the average, as the pulsed jet at  $f = 280$  Hz (Figure 11a), which equivalent  $C_q$  is estimated to be about 0.0028. Nonetheless, if the shock departures from its mean position are expressed in terms of the RMS values (Figure 11b), it is seen that the steady-state jets excite the shock motion predominantly at its root, i.e., close to the surface, approaching the uncontrolled oscillations in the outward direction. Contrary to this, the

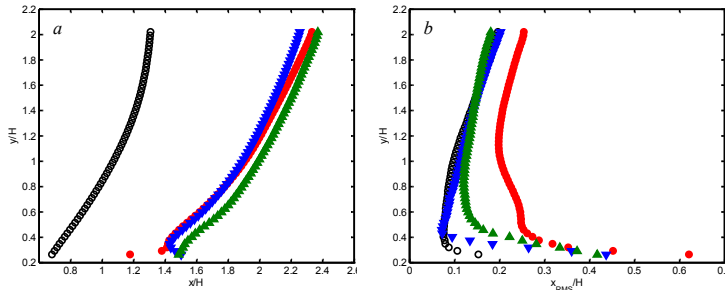


**Figure 11.** Mean shock position (a) and the RMS of the shock position fluctuations (b) for the baseline flow ( $\circ$ ,  $p_i/p_e = 1.34$ ), and the flow controlled by steady jets at  $C_q \times 10^3 = 1.7$  ( $\nabla$ ), and 2.8 ( $\triangle$ ), and by the pulsed jets at  $f = 280$  Hz and  $C_q = 0.0028$  ( $\bullet$ ).

recirculating flow is emphasized by the white contour of zero velocity. As the pulsed-jet flow control is applied, the separation point shifts downstream, and the separated domain becomes suppressed. In turn, the shock responds to the altered local pressure field and becomes displaced in the downstream direction. It should be also noted that, just as seen in Figure 4c, the shock notably slants close to the surface and the immediate downstream flow, slowed past the shock, resumes accelerating, instead of being separated.

pulsed jet excite shock displacement at much larger scales across the shock whole height, which points to significant flow control authority of the shock displacement. It should be emphasized that such a large RMS values of the shock oscillation are an artifact of both the ‘coherent’, i.e., locked to the jet cycle, and ‘incoherent’, i.e., random, motions during the shock time-dependent displacement. It is, therefore, more relevant to examine the flow response and the shock coupling to such a response with a reference to the jet oscillation cycle, i.e., ‘phase-locked’ to it.

The flow field, including the shock dynamics, is nominally resolved by PIV over forty phases of the full actuation period during any pulsed-jet cycle. An illustration of the phase-resolved shock dynamics is shown in Figure 12, where six characteristics phases of the flow field, measured by the PIV, are shown in terms of the contour plots of the streamwise velocity component. Just after the actuation signal is enabled (Figure 12a), the flow is separated far upstream, and the recirculating domain is clearly captured within the measured field of view. Shortly afterwards (Figure 12b), the shock still moves upstream, along with the flow separation, due to the inherent delay in the jet expulsion, as already discussed in connection with Figure 6. Once the jet begins its rapid (step-response) expulsion, the shear layer responds at the same rate, and the flow rapidly reattaches, which also induces the shock rapid displacement, depicted in Figures 12c and d. It should be also noted that the recirculating flow domain becomes suppressed in the field of view, as it is pushed further downward and downstream. The shock slant near the surface is visible, and accompanied by local reacceleration of the flow past the shock, just in the averaged flow field in Figure 10b. The flow appears to ‘dwell’ about this state afterwards, as also shown in Figure 12e. Finally, as the jet velocity decays during the inactive part of the cycle, the flow reattachment eases, and the flow begins to separate. As the separation point retreats upstream, so the shock responds in the same way and separated domain grows (Figure 12f), and it continues its upstream motion into the new actuation cycle, as already seen in Figures 12 a and b.

Analogous to the mean shock shapes and oscillation measures shown in Figure 11, the phase-averaged and the corresponding RMS fluctuations about such phase-averaged shock shapes are extracted for each of the forty

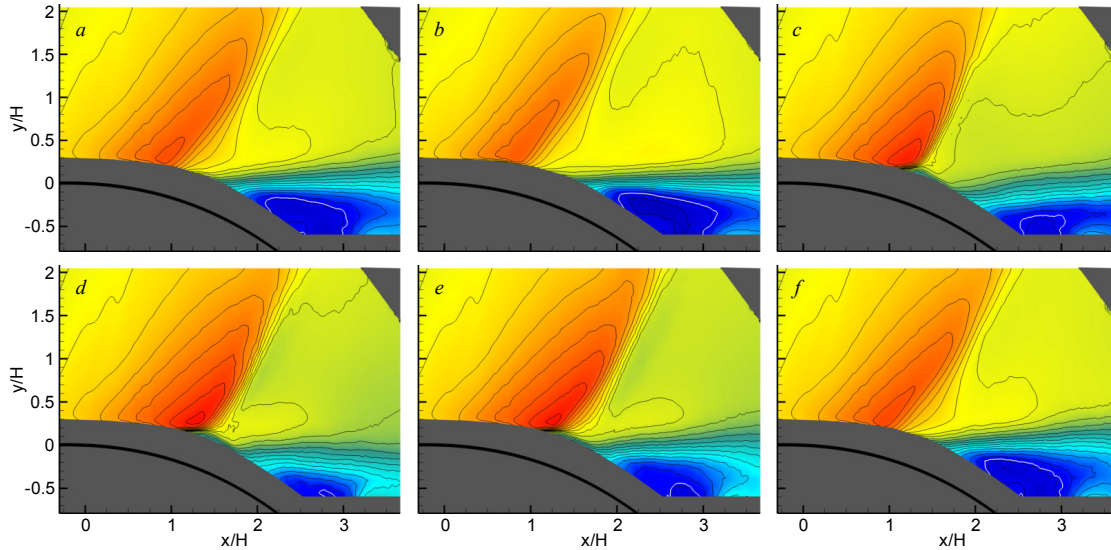


**Figure 12.** Contour plots of the streamwise velocity component for the conditionally-sampled flow field at  $t/T = 0.02$  (a), 0.17 (b), 0.29 (c), 0.39 (d), 0.49 (e), and 0.99 (f) during a single actuation cycle ( $f = 280$  Hz and  $C_q = 0.0028$ ).

resolved phases of oscillation at  $p_i/p_e = 1.34$ , and the corresponding profiles are shown in Figure 13. The baseline shock profiles and the steady jet control at equivalent  $C_q = 0.0028$  to the pulsed jet, are shown for reference. The pulsed-jets control authority is manifested through a total range of the shock motions locked to the actuation cycle over about  $\Delta x/H = 0.5$  (Figure 13a). As the actuation cycle starts, the shock is initially in the retreating motion, marked by the directional arrow, but afterwards reverses and continues its downstream displacement until it overshoots the averaged displacements of an equivalent continuous jet. As it reaches its upper limit, it weakly oscillates about that position, until it begins to retreat towards the beginning of the next actuation cycle. Once the flow control is established, the shock never reaches the baseline flow shock position, but rather oscillates between its two cycle-locked end states. Therefore, the pulsed jets not only lock the shock motion to its cycle of operation, but also impose a fixed downstream offset to its position under this operating condition. This is a result of the jet oscillation cycle at such frequency (Figure 5), namely that the jet velocity does not fully terminate at the end of the oscillation cycle; hence the finite offset in the shock position. The full range of the shock positions is accompanied with a range of its oscillations about these phase-averaged positions. Figure 14b shows a change in the RMS fluctuations about the phase-averaged positions, which suggest that the level of RMS fluctuations is related to the direction of shock motion. The RMS fluctuations appear to be more suppressed during the shock response to the onset of actuation, while it is displaced in the downstream direction (solid lines), as the flow reattaches, and the RMS fluctuations tend to increase as the flow separates, i.e., during the shock upstream displacement (dashed lines). Also, although the shock never approaches the baseline shock position (Figure 13a), the shock RMS fluctuations approach those of the baseline shock near the surface and actually become lower than the baseline RMS away from the wall during the shock downstream displacement. This indication that the shock oscillations become suppressed during its rapid displacement point to further investigation of this flow control approach for shock stabilization, especially under the higher actuation frequencies.

A fully-resolved shock motion, extracted from the phase-locked PIV measurements, during the pulsed-jets actuation cycle at  $f = 280$  Hz and  $p_i/p_e = 1.34$  is shown in Figure 14. Along the shock trajectory, the corresponding pulsed-jet velocity profile is shown, as

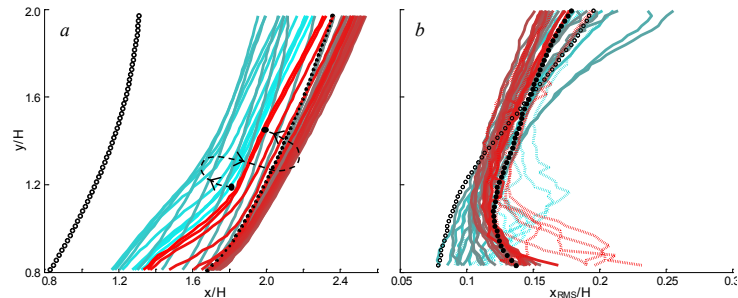


**Figure 13.** Phase-averaged shock position (a) and the RMS of the shock position fluctuations (b) for the forty equidistant phases during the pulsed jet actuation cycle ( $f = 280$  Hz,  $C_q = 0.0028$ ). The corresponding mean and RMS profiles for the baseline flow ( $\circ$ ,  $p_i/p_e = 1.34$ ), and the flow controlled by continuous jets at  $C_q = 0.0028$  ( $\bullet$ ) are shown for reference.

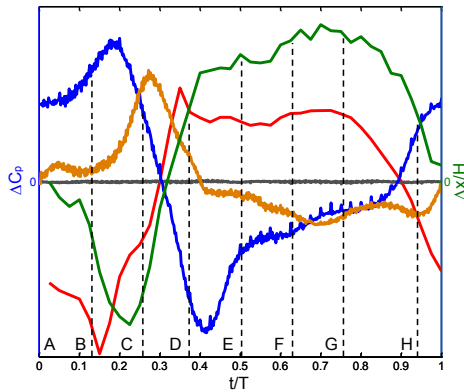


**Figure 14.** Time traces of the pulsed jet velocity (—), shock position (—), and  $p_{d1}$  (—),  $p_{d2}$  (—), and  $p_{d3}$  (—) pressure transducers during a single actuation cycle ( $f = 280$  Hz,  $p_t/p_e = 1.34$ ).

well as all the three pressure transducer traces. Several characteristic instances in time during the actuation cycle are marked on the plot as *A* through *H*. First, it is seen that the shock displacement closely follows the jet velocity evolution during the cycle, but with a pronounced phase delay. Second, a close inverse proportionality between the immediate downstream pressure trace  $p_{d2}$  and the shock displacement is noted during the full actuation cycle. The same inverse proportionality was noted, without enough resolution of the actuation cycle, in the case of the flow control by fluidic oscillating jets.<sup>36</sup> Each positive excursion in the pressure is associated with negative excursion in the shock displacement, and vice versa. As the separation of the flow becomes suppressed under the flow control, the flow accelerates further over the convex surface and the surface pressure decreases. As the coupled response of the shock displaces it downstream, i.e., in the positive direction, there is an inverse proportionality between the two. The opposite signs correspond to the flow separation during the relaxation period, when the pressure increases and the shock displaces in the negative direction. Such a clear relationship between the pressure  $p_{d2}$  dynamics and the shock

dynamics presents a two-fold advantage: the shock dynamics can be inferred from the dynamic pressure measurements, which are far simpler to conduct, and such a pressure sensor can be used for any further closed-loop control of the shock displacement and dynamics. As already discussed in conjunction with Figure 6, the upstream pressure  $p_{d1}$  is fully invariant during the actuation cycle, and it is omitted from further presentation hereafter. The second downstream pressure  $p_{d3}$  exhibits similar response to  $p_{d2}$ , with a certain phase offset and modification. As the jet is activated at  $t/T = 0.22$ ,  $p_{d3}$  continues to rise, responding to the shear layer flow from the previous actuation cycle as the current actuation effect has not propagated that far downstream. Similarly, after  $p_{d3}$  registers the flow reattachment from  $0.3 < t/T < 0.4$ , it does not exhibit any significant change until it approaches the beginning of the cycle.

A sequence of schlieren visualizations of the flow control that is conditionally sampled relative to the jet actuation period is shown in Figure 15. The actuation phase/time instances depicted in schlieren Figures 15a–h correspond to the instances marked in Figure 14 as *A* through *H*, respectively. It should be noted that the shock is not fully locked to the actuation phase, as discussed in Figure 13, and each of the images shown in Figure 15 is a representative of that state, within a band of realizations. Nonetheless, there are a number of trends related to the shear layer and shock dynamics that is elucidated from this schlieren visualization, assisted by the accompanied dynamic pressure

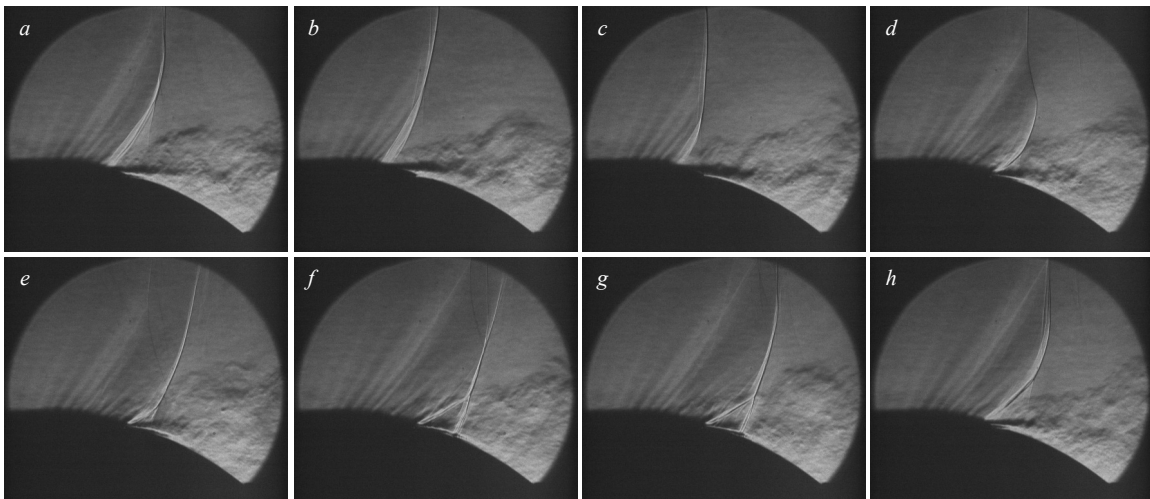


**Figure 15.** Schlieren visualization of the transonic shock at  $p_t/p_e = 1.34$  controlled by the pulsed jets at  $t/T = 0$  (a), 0.125 (b), 0.25 (c), 0.375 (d), 0.5 (e), 0.625 (f), 0.75 (g), and 0.936 (h), phase of the actuation cycle ( $f = 280$  Hz,  $C_q = 0.0028$ ).

traces (Figure 14). First, as the flow is controlled synchronously at a given  $f = 280$  Hz, the initial cycle phase at  $t/T = 0$  (Figure 15a) does not recover the unactuated flow state that was shown in Figure 7c. The flow separation remains suppressed at the beginning of the present actuation cycle relative to the baseline flow and the shear layer is visibly spread and diffused, inducing a shock displacement in the downstream direction. This is attributed to the previous actuation cycle that does not fully relax the pulsed jet velocity to zero, and the remnant effect of the previous actuation cycle is carried into the next one. The retreating shock motion continues at the next actuation phase  $t/T = 0.125$  (Figure 15b), as the pulsed jet onset lags the actuation signal, as previously shown in Figure 6. Hence, the pressure behind the shock increases, separation point moves upstream and the shock retreats in the streamwise direction, particularly further away from the surface. Also, it is seen that the shear layer regains some of its coherence. At the next phase  $t/T = 0.25$  (Figure 15c), the pulsed jet just begins to form (Figure 14), and the separation point is still upstream from the  $t/T = 0$ , while the outer shock notably lags the shock position at the beginning of the cycle. However, as the jet velocity rapidly rises past this point (Figure 14), the flow field also undergoes a rapid transition to the next phase  $t/T = 0.375$  (Figure 15d). The control jet begins to vector the separated flow and reattaches it past the separating point at the beginning of the cycle. This, in turn, lowers the pressure downstream from the shock and displaces it downstream. It is interesting to note that an artifact of the rapid shock displacement is seen in its uneven response across its height: as the shock closer to the surface rapidly responds to the altered surface pressure field, its upper part does not follow synchronously and develops an inflection point over the shock height. At  $t/T = 0.5$  (Figure 15e), the flow separation delay is further enhanced, and the shock is consequently displaced downstream up to the actuator orifice. It appears that the shock root locks to the actuator orifice at this point. However, as the flow remains vectored further downward, the shock, having its locked root, begins to slant to accommodate the flow directionality. The slanted shock weakens relative to its pseudo-normal counterpart, and the flow eventually remains supersonic past the slanted shock. As this flow can further accelerate atop of the vectored shear layer, it eventually terminates in the normal shock that induces a lambda shock root, as seen in Figure 15e. Besides the altered shock structure and dynamics, the flow remains clearly separated under the shock, as the shear layer forms at its leading leg. A clear imprint of the jet is seen along the surface, but the jet at this stage vectors the shear layer and does not fully reattach the flow. However, the following two phases depict the flow control fully established effect (Figures 15f and g). The pulsed jet is at its operating peak (Figure 14) and the separated flow becomes fully reattached. It should be noted that the jet can clearly be seen along the surface up to the trailing shock of the lambda root hence indicating the supersonic flow between the leading and the trailing shocks fully attached. Finally, as the pulsed jet begins to weaken past the phase  $t/T = 0.75$  (Figure 14), the separation delay becomes suppressed, the flow separates and the shear layer re-forms (Figure 15h). This, in turn, initially weakens the lambda structure, which is followed by a suppressed condition for its formation altogether, and the shock begins to retreat to its initial state, towards the initiation of the next actuation cycle.

Owing to the high correlation between the time-resolved downstream pressure traces and the shock displacement (Figure 14), further effects of the varying actuation frequency on the flow are examined through analysis of the responses of the surface mounted dynamic pressure sensors. The time-resolved signals from these sensors are phase averaged with respect to the trigger signal sent to the actuator array, the results of which are shown in Figure 16. In addition to the downstream pressure traces  $p_{d2}$  and  $p_{d3}$ , the trigger signal to the jets and the corresponding jet velocity profiles are superposed onto the plots. Examination of the transient effects begins with the lowest actuation frequency,  $f = 100$  Hz, where the sharp rise of the strength of the jet initially leads to a decrease in the pressure measured by both downstream pressure sensors. While the  $p_{d3}$  continues to decrease up to about  $t/T = 0.25$ ,  $p_{d2}$  reverses to an increase at  $t/T = 0.19$ , only to continue decreasing past  $t/T = 0.25$ . As the jet actuation ceases ( $t/T = 0.55$ ),  $p_{d2}$  sharply recovers, while  $p_{d3}$  follows with less of an excursion. As the actuation frequency increases, the jet transient parts of the actuation cycle begin to encompass the limit states, and a mean offset is added to their operation, such that they do not return to zero velocity at the end of the cycle. These changes clearly affect the relative response times ( $t/T$ ) of both the rise and fall of the pressure traces as the slower fall off in jet strength is reflected in the slower rise in both pressure traces (Figure 16b), and leveling of  $p_{d3}$  afterwards. As the actuation frequency is further increased, although the rise time for the jets stays nominally constant, both the rise and fall velocity times begin to take up larger periods of the actuation cycle. The corresponding pressure traces track the altered velocity shape, indicating that the flow response time is less than the actuation period. At actuation frequencies above  $f = 500$  Hz (Figure 16e), there are no more momentary quasi-steady jet intervals, as the jet velocity approaches a quasi-sinusoidal response to the step changes in the control input. Along with the jet response change,  $p_{d2}$  sensor traces follow with a quasi-sinusoidal response, which can be referenced to the jet velocity cycle, while  $p_{d3}$  response is progressively more suppressed. It is interesting to note the change in the jet velocity response



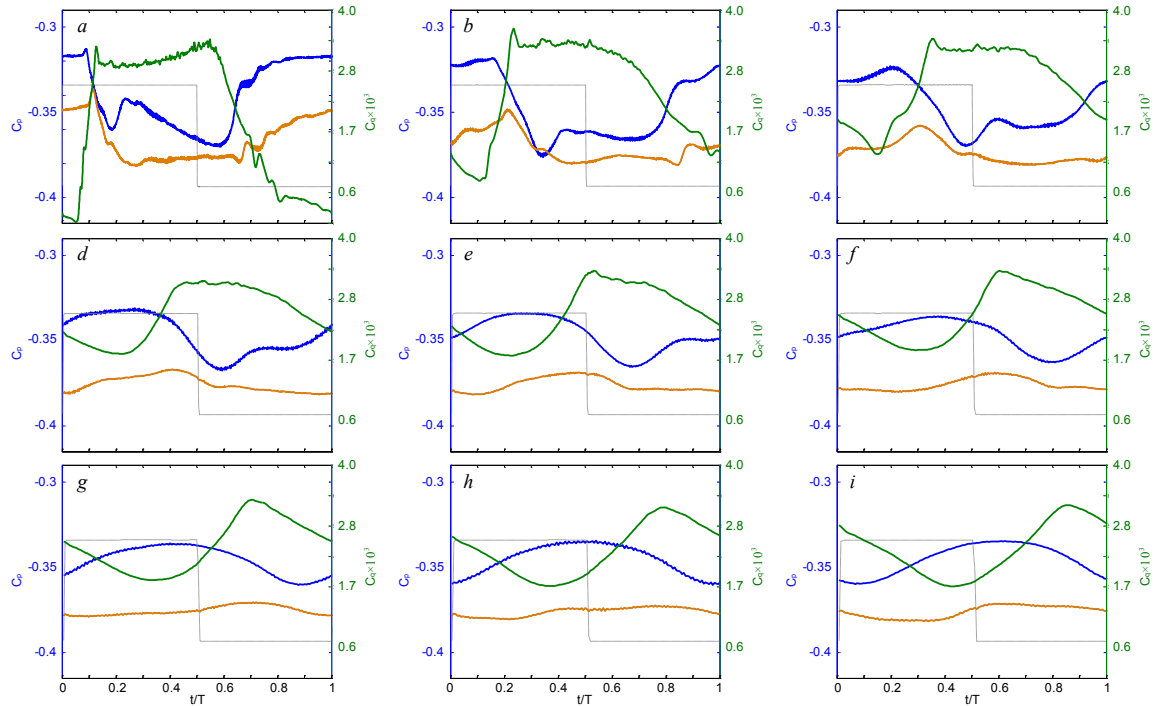


**Figure 16.** Time traces of the jet velocity ( $\rightarrow$ ),  $p_{d2}$  ( $\rightarrow$ ), and  $p_{d3}$  ( $\rightarrow$ ) during a single actuation cycle at  $f = 100$  (a), 200 (b), 300 (c), 400 (d), 500 (e), 600 (f), 700 (g), 800 (h), and 900 (i) Hz. Active half-period is shown (---) for reference

is accompanied by increasing phase lag relative to the control signal (active between  $0 < t/T < 0.5$ ), and this phase delay results in an almost fully out of phase shift between the trigger signal to the jets at the highest actuation frequency (Figure 16i). The present results indicate that this phase offset of the pulsed jets at higher operating frequencies have a twofold effect on the shock dynamics. They can be utilized for controlling the shock positioning (within realizable range). Also, as the low-amplitude pressure variations at high actuation frequencies suggest (Figures 16g–i), the higher actuation frequencies could be utilized for controlling shock oscillation within a narrow range, perhaps even its stabilization at optimal control frequencies.

As  $p_{d2}$  pressure rise is nominally associated with the flow separation (and the shock) upstream displacement, temporary pressure rise measured during the rapid flow reattachment process between  $0.19 < t/T < 0.25$  (Figure 16a) at  $f = 100$  Hz is examined closer in a series of schlieren visualizations. Figure 17 shows a sequence of schlieren images at characteristic

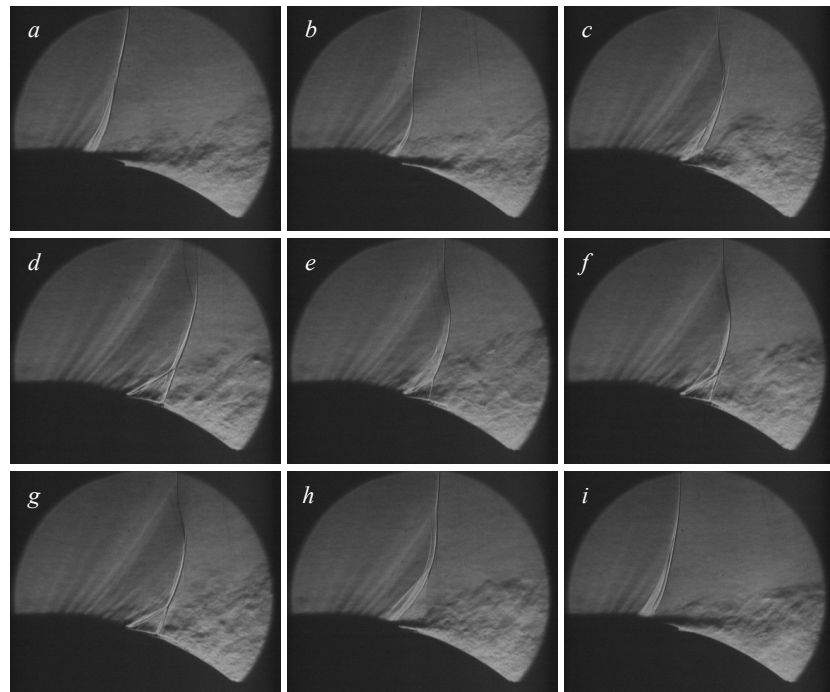


**Figure 17.** Schlieren visualization of the transonic shock at  $p_t/p_e = 1.34$  controlled by the pulsed jets at  $t/T = 0$  (a), 0.13 (b), 0.19 (c), 0.22 (d), 0.33 (e), 0.44 (f), 0.61 (g), 0.67 (h), and 0.89 (i) phase of the actuation cycle ( $f = 100$  Hz,  $C_a = 0.0028$ ).



times during the full cycle of operation of the pulsed jet at  $f = 100$  Hz, having an emphasis on the first third of the cycle. At the beginning of the actuation cycle (Figure 17a), the flow field, in principle, does not differ significantly from the baseline structure; the shock induced separation is visible closer to the geometry apex, followed by a strong shear layer and a large separated flow domain. The second phase shown in Figure 17b is selected at the local peak of the jet velocity ( $t/T = 0.13$ ), and a notable shear layer vectoring is observed, along with the shock downstream displacement and separation delay. It also appears that the rapid shock response to the altered flow field becomes somewhat delayed further away from the surface. By the next phase ( $t/T = 0.19$ ) the  $p_{d2}$  response reaches its local minimum, indicating that the flow is reattached the farthest up to that point. Indeed, the corresponding schlieren visualization (Figure 17c) points to the farthest separation delay, which is associated with the significant shear layer spreading and shock displacement. Also, the uneven shock response is still seen propagating outward, creating an inflection point in the shock shape. The next characteristic phase is selected close to the end  $p_{d2}$  local rise ( $t/T = 0.22$ ). The corresponding flow clearly shows an already formed lambda shock structure, which was already discussed in conjunction with Figure 15. Therefore, this visualization suggests that the local pressure increase is associated with formation of the downstream leg of the lambda shock, as the local flow becomes slowed down through the second shock leg, once it forms. The formation of the downstream leg occurs as the ‘virtual shape’ of the surface effected by the jets is such that the flow is accelerated downstream from the leading leg. As the flow further reattaches underneath the shock structure, and past the shock, the pressure decreases again through the phases shown in Figures 17e–g. Finally, as the actuation is terminated at about  $t/T = 0.55$ , the reattached flow begins to relax, bypassing the lambda shock condition (Figure 17h), followed by re-growth of the shear layer (Figure 17i), as the flow approaches the next actuation cycle.

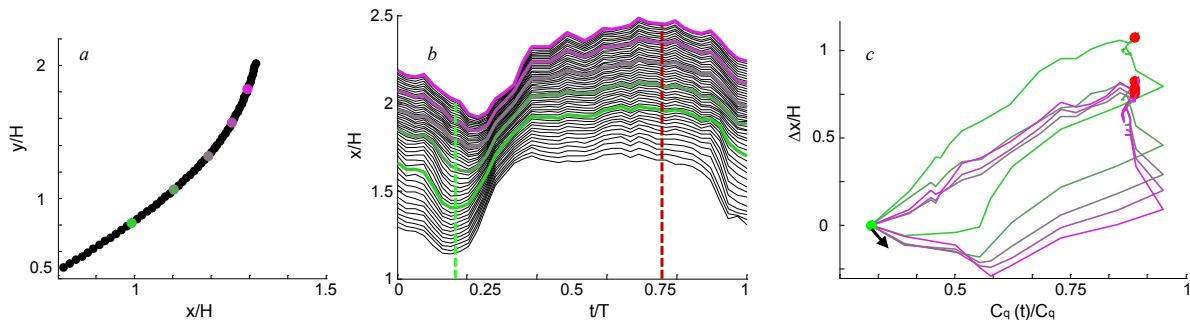


**Figure 18.** The mean baseline shock profile at  $p_t/p_e = 1.34$  (a), the ‘waterfall’ representation of phase-averaged shock displacement across its height at  $C_q = 0.0028$  (b), and the shock relative displacement with the jet relative  $C_q$  (c). The onset and termination of the jet are shown in green and red dashed lines, respectively.

The shock positions computed from the PIV flow fields are extracted and displayed in detail in Figure 18. The position of the shock wave is phase-averaged with respect to the jet actuation cycle and the streamwise position of the shock wave is displayed in Figure 18b over the jet cycle, with each line representing a particular  $y$ -elevation in a ‘waterfall’ representation. The vertical dashed green and red lines represent the onset of the jet expulsion and start of the decline in jet strength, respectively. A subset of the evolution of streamwise shock wave positions is extracted at particular  $y$  elevations, as marked on the mean shock shape shown in Figure 18a, and displayed as a function of the equivalent time-dependent  $C_q$  in Figure 18c, where time progress around the actuation cycle is in a clockwise direction as indicated by the black arrow. The green and red dots represent the points in the cycle which corresponds to the dashed vertical lines in Figure 18b. As indicated by the family of curves in Figure 18b, the shock wave does not respond in concert to the onset of the jet expulsion. While the shock responds almost immediately close to the surface, the response becomes progressively delayed in the outward direction. The same trend is more clearly shown in Figure 18c, where all five traces move upstream, for the selected five elevations, as the jet begins to discharge. As the jets momentum increases, the shock wave moves rapidly downstream, as seen in the sharp rise in the traces in Figure 18b. However, similar to the response times, the rate of change in the shock displacement varies across its height, and it decreases away from the surface. Therefore, the shock base begins to translate downstream before the rest of the shock wave. This is attributed to the propagation of the flow field changes that originate along the surface. Following the rapid downstream motion of the shock wave, as the jet reaches its limit state, the shock position remains virtually constant over a portion of the cycle illustrated in Figure 18b by the nominally flat sections between  $0.4 < t/T < 0.75$ , and also shown in Figure 18c by the clustering of points in the upper right hand region of the plot. As the jet strength declines after the beginning of the inactive part of the cycle at a less rapid rate than its onset, the shock wave motion back to its upstream position follows the decline in jet strength, a trend which is most

apparent in the fact that the shock wave position and  $C_q(t)$  becomes unique across all of the examined points, but the lowest one, indicating their synchronous response with strong correlation to the control parameter  $C_q(t)$ .

## V. Conclusions

The present experimental investigation focuses on *indirect* control of a transonic shock over a 2-D convex surface. The transonic shock forms over the aft section of the surface geometry, past the critical condition. The shock-induced thickening of the boundary layer, along with adverse pressure gradient, results in shock-induced flow separation that evolves into a large domain of the separated flow bound by the shear layer. The flow control explores the coupling between the flow separation, shear layer, and transonic shock, and is primarily focused on the shear layer vectoring and separation delay, where the shock control is achieved only indirectly through the shock response to the altered flow/pressure field. The pulsed jets are utilized as fluidic flow control elements that are distributed across the flow span upstream, and actuated synchronously at frequencies up to 900 Hz.

The characteristics of both the baseline and controlled flows are assessed using several diagnostic tools. Global features of the flow fields and the shock dynamics are elucidated from the conditionally-sampled schlieren visualization where the field of view is centered about the aft section of the ramp. Static pressure measurements are used for characterization of the baseline flow (in the absence of actuation), and dynamic pressure measurements are utilized for time-resolved changes in surface pressure distributions upstream and downstream from the shock. A particular emphasis is placed on correlations between the surface pressure in the separated flow domain and the unsteady shear layer and shock dynamics. Finally, high-speed (2,800 fps) PIV measurements in a cross-stream plane provide information about the time- and phase-averaged flow fields, as well as the corresponding shock dynamics, which are extracted from the measured flow fields.

Baseline flow analysis shows the flow evolution as it approaches the critical condition for shock formation: subsonic flow separation due to adverse pressure gradient becomes somewhat displaced upstream at the initial shock formation due to the boundary layer thickening, and soon afterwards couples to the shock root. Such a coupling between the flow separation point, shock, and the incipient shear layer, enables alteration of all of these entities by perturbations of any of them. As the oncoming flow Mach number is increased past the critical point, the transonic shock becomes displaced in the downstream direction and alters its shape from an initially normal shock to a more oblique shock. Consequently, the shock weakens somewhat near its root, but gains in strength away from the surface.

It is shown that the pulsed flow actuation leads to a momentary attachment of the separated shear layer. This, in turn, alters the pressure field and effects a significant synchronized streamwise translation of the shock, which is then followed by a longer relaxation as the surface vorticity layer re-separates over the jet inactive portion of the actuation cycle. Following the rapid displacement and distortion during the transitory onset of the actuation, nominally normal shock intensifies and transitions to lambda shock when the actuation jets reach their full momentum. The emergence of the lambda shock structure is attributed to shock locking to the separation point, while the increasing jet momentum continues to vector the shear layer and upper flow. Therefore, the shock near the surface slants to accommodate increasing flow vectoring, thereby also becoming weaker. At the point that the flow past the weakened shock is still supersonic, it further accelerates and eventually terminates in a normal shock that forms the downstream leg of the lambda shock structure. Although the flow initially remains separated off the leading leg of the lambda shock, the full jet momentum is capable of fully attaching the flow underneath the lambda shock and even further downstream from the shock. The present data show an excellent correlation between the surface dynamic pressure and the shock position that is extracted from the PIV measurements, which suggest a good candidate for potential closed-loop control of the shock motion. Furthermore, when the actuation is applied with a given jet velocity offset, the shock's nominal position is offset relative to the baseline flow (i.e., in the absence of actuation), and it continues to respond to time-dependent actuation relative to the offset position. These findings indicate that indirect control of shock induced separation can be further exploited for shock stabilization and time-dependent positioning.

## Acknowledgment

This work has been supported by the Air Force Research Laboratory (AFRL).

## References

- <sup>1</sup>Pearcey, H.H., "Shock-Induced separation and its prevention by design and boundary layer control," Boundary Layer and Flow Control Vol. 2, pg1166-1349. Pergamon Press, 1961.

- <sup>2</sup>Delery, J.M., "Shock Wave/Turbulent Boundary Layer Interaction and its Control," Prog. Aerospace Sci., Vol. 22, 1985, pp. 209-280.
- <sup>3</sup>Viswanath, P.R., "Shock-Wave-Turbulent-Boundary-Layer Interaction and its Control: A Survey of Recent Developments," Sadhana, Feb., 1988, pp. 45-104.
- <sup>4</sup>Bushnell, D. M., "Shock Wave Drag Reduction," Annual Review of Fluid Mechanics, Vol. 36, 2004, pp. 81-96.
- <sup>5</sup>Ferri A., "Experimental Results with Airfoils Tested in the High-Speed Tunnel at Guidonia", Atti. DiGuidonia, No. 17, 1939, Eng. Trans. 1940.
- <sup>6</sup>Liepmann, H.W., "Interaction between boundary layer and shock waves in transonic flow," Journal of Aeronautical Sciences, Vol. 13, 1946, pp. 623-637.
- <sup>7</sup>Ackeret, J., Feldmann, F., and Rott, K., "Investigations of Compression Shocks and Boundary Layers in Gases Moving at High Speed," NACA TM 1113, 1947.
- <sup>8</sup>Liepmann, H.W.; Roshko, A.; and Dhawan, S., "On reflection of shock waves from boundary layers," National Advisory Committee for Aeronautics, Report 1100, 1951, pp. 889-917.
- <sup>9</sup>Adamson, T.C. Jr. and Messiter, A.F., "Analysis of Two-Dimensional Interactions Between Shock Waves and Boundary Layers," Annual Review of Fluid Mechanics, Vol. 12, 1980, pp. 103-138.
- <sup>10</sup>Andreopoulos, J. and Muck, K.-C., "Some New Aspects of the Shock-Wave/Boundary-Layer Interaction in Compression-Ramp Flows," Journal of Fluid Mechanics, Vol. 180, 1987, pp. 405-428.
- <sup>11</sup>Liu, X., and Squire, L.C., "An Investigation of shock/boundary-layer interactions on curved surfaces at transonic speeds." J. Fluid Mec. Vol 187. Pg. 467-486. 1988.
- <sup>12</sup>Delery, Jean M. "Experimental Investigation of Turbulence Properties in Transonic Shock/Boundary-Layer Interactions." AIAA Journal. Vol. 21 No. 2. pg 180-185. 1983.
- <sup>13</sup>Sartor, Fulvio, Losfeld, Gilles. Bur, Reynald. "PIV study on a shock-induced separation in a transonic flow." Exp. Fluids. DOI 10.1007/s00342-012-1330-4.
- <sup>14</sup>Baresh, Steven J. Henfling, John F. Spillers, Russell W. Pruett, Brian O. "Unsteady Shock Motion in a Transonic Flow over a Wall-Mounted Hemisphere." AIAA Paper, AIAA 2013-3201, June 2013.
- <sup>15</sup>Poggie, Jonathan., Bisek, Nicholas J. Kimmel, Roger L. "Spectral Characteristics of Separation Shock Unsteadiness" AIAA Paper, AIAA 2013-3203, June 2013.
- <sup>16</sup>Pearcy, HH. Holder, DW. "Examples of the Effects of Shock-Induced Boundary Layer separation in Transonic Flight." Ministry of Technology, ARC, R&M No. 3510. January 1954.
- <sup>17</sup>Dolling, D.S., "Fifty Years of Shock-Wave/Boundary-Layer Interaction Research: What Next?," AIAA Journal, Vol. 39, No. 8, 2001, pp. 1517-1531.
- <sup>18</sup>Lin, J.C., "Review of research on low-profile vortex generators to control boundary-layer separation," Progress in Aerospace Sciences, Vol. 38, 2002, pp. 389-420.
- <sup>19</sup>Ashill, P.R., Fulker, J.L., and Hackett, K.C., "Research at DERA on Sub Boundary Layer Vortex Generators (SBVGs)," AIAA Paper AIAA-2001-0887, Jan, 2001.
- <sup>20</sup>Barter, J.W., Dolling, D.S., "Experimental Study of the Use of Vortex Generators to Reduce Fluctuating Pressure Loads in Shock Wave Turbulent Boundary Layer Interactions." AIAA Paper AIAA-1993-4335, Oct, 1993.
- <sup>21</sup>Lee, B.H.K. "Self-sustained shock oscillations on airfoils at transonic speeds" Progress in Aerospace Sciences. Volume 37. 147-196. 2001.
- <sup>22</sup>Gaitonde, D.V. "Progress in Shock Wave/Boundary Layer Interactions," AIAA Paper, AIAA- 2013-2607, June 2013.
- <sup>23</sup>Stanewsky, E., Delery, J.; Fulker, J.; Matteis, P. de (Editors). "Drag Reduction by Shock and Boundary Layer Control", Springer, 2002.
- <sup>24</sup>Holden, H. and Babinsky, H., "Effect of Microvortex Generators on Separated Normal Shock/Boundary Layer Interactions," Journal of Aircraft, Vol. 44, No.1, 2007, pp. 170-174.
- <sup>25</sup>Lee, S., Loth, E., and Babinsky, H., "Normal Shock Boundary Layer Control with Various Vortex Generator Geometries," Computers and Fluids, Vol. 49, 2011, pp. 233-246.
- <sup>26</sup>Gordeyev, S., Burns, R., Jumper, E., Gogineni, S, Paul, M., and Wittich, D., "Aero-Optical Mitigation of Shocks Around Turrets at Transonic Speeds Using Passive Flow Control", AIAA Paper AIAA-2013-0717, Jan 2013.
- <sup>27</sup>Wallis, R.A., Stuart, C.M. "On the Control of Shock-Induced Boundary-Layer Separation with Discrete Air Jets." Ministry of Aviation Aeronautical Research Council. C.P. No. 595, February, 1958.
- <sup>28</sup>Englar, Robert J. "Two-Dimensional Transonic Wind Tunnel Tests of Three 15-percent Thick Circulation Control Airfoils." NSRDC, Technical Note AL-182, December 1970.

- <sup>29</sup>Krogmann, P., Stanewsky, E., and Thiede, P., “Effects of Suction on Shock/Boundary-Layer Interaction and Shock-Induced Separation,” *Journal of Aircraft*, Vol. 22, No.1, 1985, pp. 37-42.
- <sup>30</sup>Souverein, L.J. and Debieve, J.-F., “Effect of Air Jet Vortex Generators on a Shock Wave Boundary Layer Interaction,” *Experiments in Fluids*, Vol. 49, 2010, pp. 1053-1064.
- <sup>31</sup>Kalra, C.S, Shneider, M.N., and Miles, R.B., “Numerical Study of Boundary Layer Separation Control Using Magnetogasdynamic Plasma Actuators,” *Physics of Fluids*, Vol. 21, 2009, 106101.
- <sup>32</sup>Kalra, C.S, Zaidi, S.H., Miles, R.B., and Macheret, S.O., “Shockwave–Turbulent Boundary Layer Interaction Control Using Magnetically Driven Surface Discharges,” *Experiments in Fluids*, Vol. 50, 2011, 547-559.
- <sup>33</sup>Narayanaswamy, V., Clemens, N.T., and Raja, L.L., “Investigation of a Pulsed-Plasma Jet for Shock / Boundary Layer Control,” *AIAA Paper* 2010-1089, Jan, 2010.
- <sup>34</sup>Babinsky, Holger. Harvey, John K. “Shock Wave-Boundary-Layer Interactions,” Cambridge University Press, 2011.
- <sup>35</sup>Vukasinovic, B. Gissen, A.N., Glezer, A., and Gogineni, S. “Fluidic Control of Transonic Shock-Induced Separation,” *AIAA Paper* AIAA-2013-0529.
- <sup>36</sup>Gissen, A.N., Vukasinovic, B., Glezer, A., and Gogineni, S. “Active Shock Control in a Transonic Flow,” *AIAA Paper* AIAA-2013-3116.